Research Square

Preprints are preliminary reports that have not undergone peer review.
They should not be considered conclusive, used to inform clinical practice,
or referenced by the media as validated information.

# Orientation Mechanics and Kinetic Constraints of In-Situ Low-Field Magnetic Alignment in Vat Photopolymerization

**Shannon T. O. Thomsen**
**Habiba Bougherara**
habiba.bougherara@torontomu.ca

Toronto Metropolitan University Faculty of Engineering & Architectural Science https://orcid.org/0000-0001-6678-570X

**Research Article**

**Keywords:** Vat photopolymerization, Helmholtz coils, Microstructure orientation, Anisotropic microfillers, Magnetic alignment, Viscous drag kinetics

**Posted Date:** October 13th, 2026

**DOI:** https://doi.org/10.21203/rs.3.rs-11199912/v1

**License:** This work is licensed under a Creative Commons Attribution 4.0 International License.
Read Full License

# Orientation Mechanics and Kinetic Constraints of In-Situ Low-Field Magnetic Alignment in Vat Photopolymerization


## Authors

Shannon T. O. Thomsen[1], Habiba Bougherara[1],*

[1] Toronto Metropolitan University
Department of Mechanical Engineering
87 Gerrard St E, Toronto, ON M5B 1G8, Canada

*Corresponding author: Habiba Bougherara
Email address: habiba.bougherara@torontomu.ca

ORCID(s)
Shannon T. O. Thomsen: 0009-0003-4311-3347
Habiba Bougherara: 0000-0001-6678-570X



## Abstract

In-situ magnetic alignment of microfillers during vat photopolymerization (VP) offers a route to fabricating functional composites, but electromagnetic hardware retrofits introduce significant spatial, kinematic, and thermal trade-offs. This technical note evaluates the operational boundaries of a low-field Helmholtz coil retrofitted to a commercial liquid crystal display (LCD)-based VP printer. Despite single-particle models predicting sufficient torque to overcome viscous drag, active-field operation (0.31-0.40 mT) yielded modest directional alignment ($S_{2D} = 0.156 \pm 0.104, R^2 = 0.60 \pm 0.26$, across $N = 5$ samples, 10 total region of interests (ROIs), 0.092 wt% / 0.038 vol%) compared to isotropic controls ($S_{2D} = -0.004 \pm 0.044, R^2 = 0.45 \pm 0.15$). This work delivers two key contributions: (1) it establishes that low-field conditions (0.31–0.40 mT) mark the lower sensitivity threshold required to initiate weak, statistically verifiable microscale directional bias above background noise, while quantifying the substantial field deficit relative to the ~15–50 mT needed for macro-scale functional anisotropy, and (2) it presents an analytical framework decoupling physical order parameters ($S_{2D}$) from distribution curve fitting ($R^2$), demonstrating that fit accuracy alone cannot confirm alignment. Primary performance bottlenecks-including fibre agglomeration, field magnitude deficits, and rapid particle sedimentation restricting printing to single layers-are quantified to provide critical engineering scaling criteria for future high-field magnetic additive manufacturing systems.



## Keywords

Vat photopolymerization, Helmholtz coils, Microstructure orientation, Anisotropic microfillers, Magnetic alignment, Viscous drag kinetics

## Abbreviations

UV - ultraviolet
FEP - fluorinated ethylene propylene
LCD - liquid crystal display
PCFs - precision chopped fibres
PETG - polyethylene terephthalate glycol
ROI - region of interest
VP - vat photopolymerization

## 1 Introduction

In-situ magnetic alignment of anisotropic microfillers during vat photopolymerization (VP) enables the fabrication of customized, directionally functionalized polymer composites [1]. Coating non-magnetic conductive inclusions, such as precision chopped fibres (PCFs), with thin ferromagnetic coatings (e.g., nickel or iron oxide) imparts a rotational magnetic moment without compromising overall composite performance [2]. Compared to electrical or acoustic alignment methods, magnetic fields operate without direct physical contact, permeate optically dense resins, and act globally across the entire build area [3]. Consequently, field-assisted composite manufacturing and magnetic smart materials have gained widespread interest for programming directional material anisotropy prior to matrix curing, as well as enabling remote, non-contact actuation in soft robotic systems [4]. Magnetic field-assisted stereolithography has been previously demonstrated for assembling micro/nanoparticles to construct functional, multimaterial, and bioinspired hierarchical surface structures [5].

Despite the theoretical viability of field-induced orientation, retrofitting dual-coil electromagnetic hardware, specifically Helmholtz configurations [1], into compact commercial desktop VP platforms introduces significant engineering, physical, and thermal trade-offs. While the governing mechanics of particle torque are well established, the practical operational limits of in-situ magnetic VP retrofits remain under-documented in literature. Key hardware and physical constraints include:

- **Geometric & Optical Path Boundaries:** Retrofitting the size of air-core coils around small-footprint resin vats without causing physical collisions during $z$-stage travel or obscuring the bottom-up ultraviolet (UV) projection window.
- **Thermal & Rheological Limits:** Managing coil resistive heating ($I^2R$), which risks premature thermal crosslinking of the liquid photopolymer resin or structural deformation of resin vat components [3].
- **Hydrodynamic vs. Magnetic Constraints:** Overcoming viscous drag ($\tau_{\text{drag}}$) and suppressing inter-particle agglomeration/gravitational sedimentation within the narrow photopolymer gelation window under constrained field magnitudes [1].

This technical note provides a system-level engineering analysis of a low-field Helmholtz coil configuration retrofitted to a commercial liquid crystal display vat photopolymerization (LCD-VP) printer (Elegoo Mars). Rather than demonstrating an optimized material system, this work defines the critical operating boundaries, spatial/thermal limits, and governing failure modes,

specifically field magnitude deficits (0.31-0.40 mT), rapid particle sedimentation, and magnetic agglomeration. By quantifying these design constraints, this note establishes concrete criteria and design bounds for future field-assisted additive manufacturing systems. While high-degree fibre alignment ($S_{2D} > 0.50$) has been reported in specialized magnetic printing, the diagnostic boundaries and statistical reliability of dilute active-field alignment remain insufficiently characterized. The novelty of this work lies in quantifying the transition regime between complete isotropic randomness ($S_{2D} = -0.004 \pm 0.044$) and low-to-moderate active-field alignment ($S_{2D} = 0.156 \pm 0.104$). By evaluating micro-scale fibre orientation across multi-region samples, this note establishes a standardized baseline for identifying weak directional bias in photopolymer vats and highlights the critical necessity of using tensor-based orientation parameters ($S_{2D}$) [6] alongside standard distribution metrics ($R^2$).

## 2 System Architecture and Hardware Integration

### 2.1 Platform Retrofitting & Non-Magnetic Modification

Integrating electromagnetic hardware into a commercial LCD-VP platform requires maintaining $z$-stage travel clearances, unobstructed bottom-up UV light delivery, and non-magnetic structural integrity. Custom poly-lactic acid or polyethylene terephthalate glycol (PETG) mounting brackets were designed to secure a dual-coil assembly directly around the resin vat of an Elegoo Mars platform. To eliminate localized magnetic flux distortion and field asymmetry within the active print zone, standard ferromagnetic steel-alloy vat clamps were replaced with reverse-engineered, non-magnetic PETG clamps.

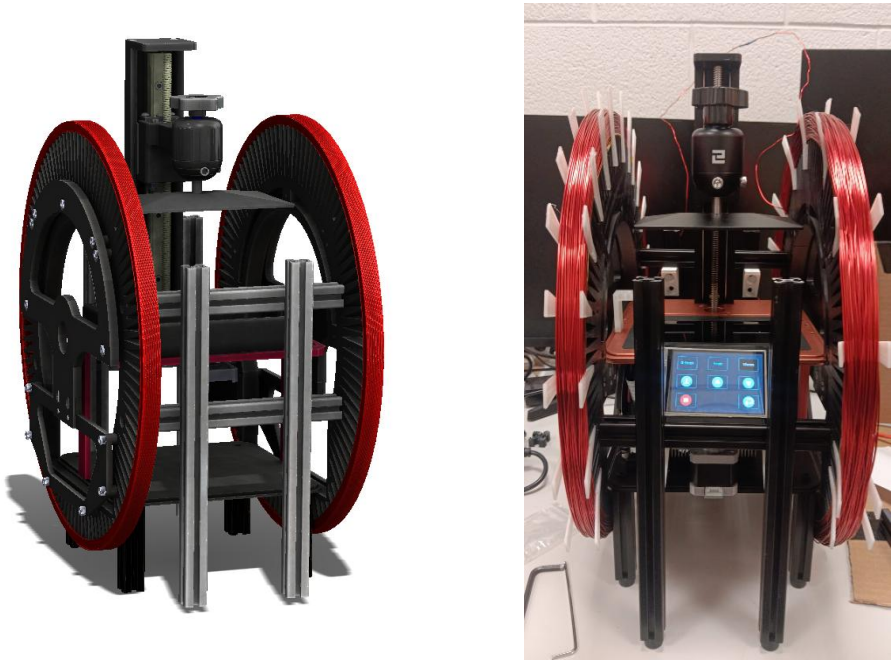

**Fig. 1** System computer-aided design (left) and physical retrofit architecture (right). The setup requires additional PETG brackets, non-magnetic clamps, and replacement of all steel bolts with Aluminum bolts, while the dual air-core coils sit around the Elegoo Mars vat without obstructing the LCD path or $z$-stage.

### 2.2 Electromagnetic Specifications and Thermal-Rheological Characterization

Air-core Helmholtz coils were wound using AWG 18 polyimide-insulated copper magnet wire to fit the machine footprint without encroaching on the optical path or build head trajectory.

**Table 1** Retrofitted Low-Field Helmholtz Coil and Material Specifications.

| **Parameter** | **Specification / Measured Value** |
|---|---|
| Base Printer Platform | Elegoo Mars 1 (LCD-VP) |
| Coil Configuration | Dual Air-Core Helmholtz Setup ($R = 182mm, N = 255\ turns/coil$) |
| Wire Type and Insulation | AWG 18 Enameled Magnet Wire with Polyimide Wrapping |
| Operating Voltage ($V$) / Current | $24\ \text{V} - 30\ \text{V DC} / 1.94\ \text{A} - 2.44\ \text{A}$ |
| Experimental Centre Field Flux Density ($B$) | $0.31 - 0.40\ mT$ |
| Functional Filler | Nickel-Coated Precision Chopped Fibres (Ni-PCFs) |
| Fibre Dimensions | $d = 7.5\mu m, L = 0.5mm$ |
| Vat Clamp / Bracket Material | Non-Magnetic PETG |
| Specimen thickness | Single-layer |

To evaluate the potential thermal impact of coil heat dissipation on the printing environment, the thermal performance of the air-core coils was characterized under continuous 30 V DC excitation (2.44 A). Under active forced-air cooling, the coil surface temperature stabilized at an equilibrium value of 42.3°C after 18 minutes. While this $I^2R$ resistive heating provided localized warming near the vat boundary, thermal monitoring confirmed that it was insufficient to induce uniform heating across the entire exposure plane prior to photopolymer gelation.

## 3 Kinematic Modeling and Alignment Boundaries

### 3.1 Balance of Magnetic Torque and Viscous Drag

To evaluate fibre rotation feasibility prior to photopolymer gelation, hydrodynamic and magnetic kinetics were modeled analytically. The net torque acting on a cylindrical fibre during rotational alignment in a liquid photopolymer is governed by the balance between magnetic dipole torque ($\tau_{\text{mag}}$) and rotational viscous drag ($\tau_{\text{drag}}$):

$$\tau_{\text{mag}} = \frac{V \cdot \Delta\chi \cdot B^2}{2\mu_0} \sin(2\theta)\ [2] \tag{1}$$

$$\tau_{\text{drag}} = \frac{\pi \cdot \eta \cdot L^3}{3[\ln(L/d) - 0.8]} \cdot \frac{d\theta}{dt}\ [7] \tag{2}$$

where $V$ is fibre volume, $\Delta\chi$ is effective magnetic susceptibility anisotropy, $\eta$ is resin dynamic viscosity, $L$ is fibre length, $d$ is fibre diameter, $\mu_0$ is vacuum permeability, $\theta$ is the angle between the fibre longitudinal axis and the magnetic field vector, and $B$ is central flux density [2][7] . Unlike

methods that manipulate mobile magnetic nanoparticles during early-stage resin gelation to form static surface features [5], continuous low-field alignment of high-aspect-ratio fibres must overcome significant rotational viscous drag ($\tau_{\text{drag}}$) prior to matrix crosslinking.

To generalize these hydrodynamic and magnetic trade-offs, rotational dynamics are expressed via the dimensionless Mason number ($Mn$), representing the ratio of viscous shear forces to magnetic dipole forces:

$$Mn = \frac{\eta \cdot \dot{\gamma}}{\mu_0 \cdot M^2} \text{ [3][8]} \tag{3}$$

where $\dot{\gamma}$ is the local shear rate and $M$ is the induced fibre magnetization ($M = \Delta\chi \cdot B/\mu_0$) [8] . For field-induced orientation to dominate before polymer crosslinking initiates, the system must operate below a critical threshold ($Mn < Mn_{\text{crit}}$). Under current experimental conditions ($\eta \approx 0.35$ Pa · s, $B = 0.40$ mT), the calculated Mason number lies two orders of magnitude above $Mn_{\text{crit}}$, confirming mathematically that viscous drag forces dominate the kinetic regime.

### 3.2 Rotational Response Time & Gelation Kinetics

Equating $\tau_{\text{mag}} = \tau_{\text{drag}}$ and integrating yields the estimated time ($\Delta t_{\text{align}}$) required for a fibre to rotate from an initial orientation ($\theta_0 \approx 45°$) to an aligned state ($\theta \approx 5°$):

$$\Delta t_{\text{align}} = \frac{2\mu_0 \cdot \pi \cdot \eta \cdot L^3}{3 \cdot V \cdot \Delta\chi \cdot B^2 [\ln(L/d) - 0.8]} \ln\left(\frac{\tan\theta_0}{\tan\theta}\right) \text{ [1]} \tag{4}$$

While ideal single-particle calculations suggested rotation times within the pre-cure window, experimental implementation revealed that actual alignment kinetics far exceeded vat photopolymerization layer gelation limits.

## 4 Experimental Validation and Failure Analysis

### 4.1 Magnetic Field Characterization

Preliminary magnetic field validation was conducted at the central exposure plane ($B_{\text{center}}$) using a 3-axis solid-state magnetometer to assess current scaling across the operational power envelope (0 V to 31 V). Baseline ambient background flux density was recorded at 23.5 $\mu$T. As shown in **Fig. 2**, the net empirical flux density ($B_{\text{net}}$) exhibited exceptional internal linearity ($R^2 > 0.99$), reaching 0.31 mT at 24 V (1.94 A) and 0.40 mT at 30 V (2.44 A).

While experimental measurements confirm linear inductive behavior, the empirical slope (0.163 mT/A) operates at roughly 13% of ideal analytical Biot-Savart predictions (1.26 mT/A for $N_{\text{coil}} = 255$ turns/coil). This efficiency offset is attributed to spatial winding dispersion across the finite coil cross-section, packing-factor losses, and unconfined air-core flux leakage within the compact desktop printer frame. Crucially, even under maximum power input (31 V / 2.53 A yielding 0.41 mT), the net generated field remains nearly two orders of magnitude below the critical threshold required for dynamic fibre alignment ($B_{\text{crit}} \approx$ 15-50 mT).

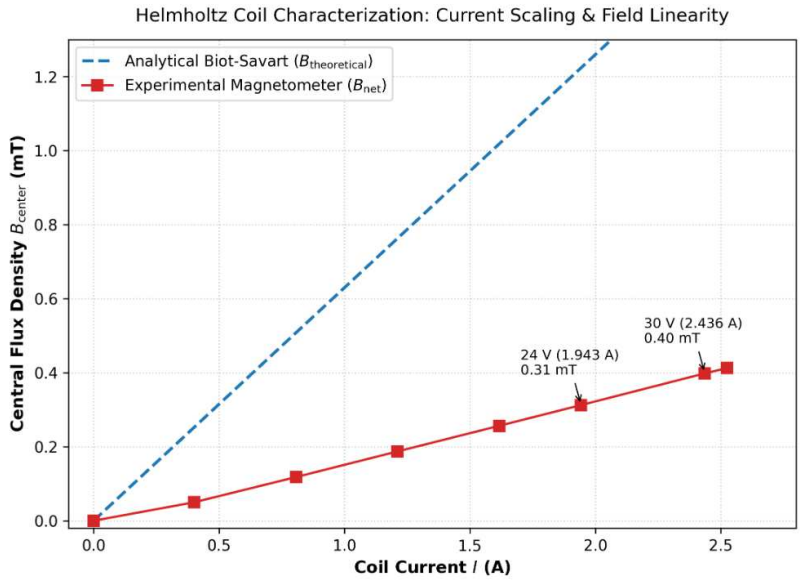


**Fig. 2** Empirical current scaling and central magnetic flux density characterization of the retrofitted dual-coil Helmholtz system.

### 4.2 Microstructure, Orientation Analysis, and Sedimentation Modes

Microstructural inspection of cross-sectioned cured single-layer composite samples via optical microscopy confirmed an isotropic fibre distribution.

Directionality histograms were generated using the ImageJ/Fiji Directionality plugin based on the Fourier components method, where a unimodal Gaussian distribution was fitted to extract the preferred direction $\theta_0$ angular dispersion $\sigma$ relative amount, and goodness of fit $R^2$. The analysis yielded a primary direction peak of $\theta = 3.60°$ with an orientation fraction of Amount $= 0.08$ and a Gaussian goodness of fit $R^2 = 0.42$. The broad, uniform baseline distribution across the angular spectrum confirms the absence of preferred orientation, and the lower Gaussian goodness of fit ($R^2 = 0.42$) reflects a multimodal/isotropic distribution that deviates from a single Gaussian peak, rather than a degradation in local fibre quality

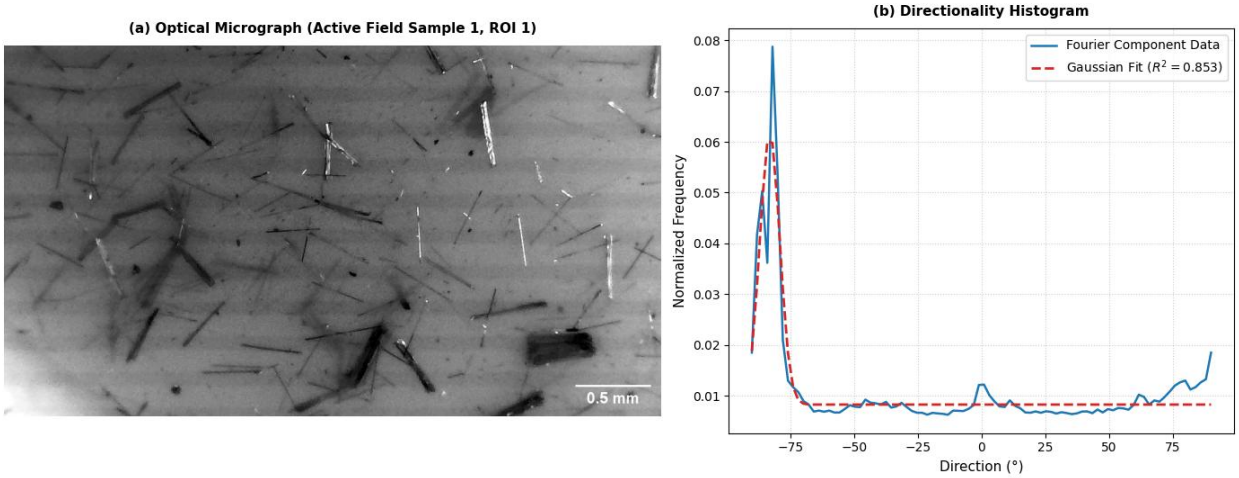

**Fig. 3** (a) Representative optical micrograph of an active-field sample (Active Field 1, ROI 1; 0.092 wt% / 0.038 vol%) showing dispersed Ni-PCFs (scale bar = 0.5 mm); quantitative directionality analysis was performed on unmanipulated raw Fourier frequency spectra. (b) Corresponding Fourier component directionality distribution and primary Gaussian fit for a single specific ROI (ROI1, $R^2 = 0.853$, peak at $\theta_0 = -83.5°$), demonstrating local preferred orientation alongside dispersed isotropic background fibres.

It should be noted that while the Gaussian goodness of fit ($R^2$) indicates the degree to which the orientation distribution adheres to a single unimodal Gaussian peak, the physical anisotropy of the fibre array is quantified by the second-order 2D orientation parameter ($S_{2D}$) [6]. In this paper, $S_{2D}$ reflects the alignment relative to the local mean vector ($\theta_0$) rather than the absolute target magnetic axis. Fibre orientation was evaluated across $N = 5$ independent active-field samples (2 ROIs per sample, 10 ROIs total) containing $0.092 \pm 0.026$ wt% ($0.038 \pm 0.011$ vol%) fibre loading over 90 angular bins. The active-field group demonstrated a preferred direction of $\theta_0 = -9.6° \pm 37.6°$, an angular dispersion of $\sigma = 11.16° \pm 14.42°$, a goodness of fit of $R^2 = 0.60 \pm 0.26$, and a second-order orientation parameter of $S_{2D} = 0.156 \pm 0.104$ relative to local preferred directions. In contrast, unaligned control samples ($N = 1$ sample, 2 ROIs; 0.110 wt% / 0.040 vol%) exhibited near-zero anisotropy ($S_{2D} = -0.004 \pm 0.044, R^2 = 0.45 \pm 0.15$), confirming an isotropic fibre distribution. These results demonstrate measurable, low-to-moderate directional anisotropy in the presence of the active magnetic field relative to unaligned controls, while high angular dispersion indicates that further field optimization is required to achieve high-degree unidirectional alignment.

**Table 2** Summary of reported values.

| Condition/Group | Fibre Loading (wt%) | Fibre Loading (vol%) | Sample Size | Preferred Direction ($\theta_0$) | Angular Dispersion ($\sigma$) | Second-Order Parameter ($S_{2D}$)[a] | Goodness of fit ($R^2$) |
|---|---|---|---|---|---|---|---|
| Control Group | 0.110% | 0.040% | N = 1 , 2 ROIs | $32.4° \pm 58.5°$ | $4.89° \pm 3.09°$ | $-0.004 \pm 0.044$ | $0.45 \pm 0.15$ |
| Active Field Group | $0.092 \pm 0.026$% | $0.038 \pm 0.011$% | N = 5, 2 ROIs | $-9.6° \pm 37.6°$ | $11.16° \pm 14.42°$ | $0.156 \pm 0.104$ | $0.60 \pm 0.26$ |

[a] $S_{2D}$ is calculated relative to the primary fitted/peak direction ($\theta_0$).

The observed results ($S_{2D} = 0.156 \pm 0.104$ vs. $S_{2D} = -0.004 \pm 0.044$) provide fundamental insight into low-field rotational kinetics. From an engineering standpoint, this provides new knowledge regarding the sensitivity limits of Fourier-component directionality analysis: a moderate Gaussian fit ($R^2 = 0.60 \pm 0.26$) under weak magnetic fields does not automatically indicate high structural anisotropy. The substantial angular dispersion ($\sigma = 11.16° \pm 14.42°$) highlights that local boundary drag and field non-uniformities dominate rotational resistance at dilute volume fractions (0.038 vol%), defining the precise threshold where active magnetic torque overcomes resin viscous resistance.

In addition to rotational inhibition, Ni-PCFs displayed rapid gravitational settling ($v_s$) due to the density differential between the nickel-coated fibres ($\rho \approx 8.9$ g/cm$^3$) and the photopolymer matrix ($\rho \approx 1.1$ g/cm$^3$). Particles settle rapidly along the $z$-axis ($v_s$), accumulating into a dense, randomly oriented sediment layer ($S \approx 0$) against the fluorinated ethylene propylene (FEP) film prior to UV

exposure. Concurrently, this high-density sediment layer creates an optical barrier that prevents effective UV light penetration past the initial layer, effectively restricting printing operations to single-layer geometries.

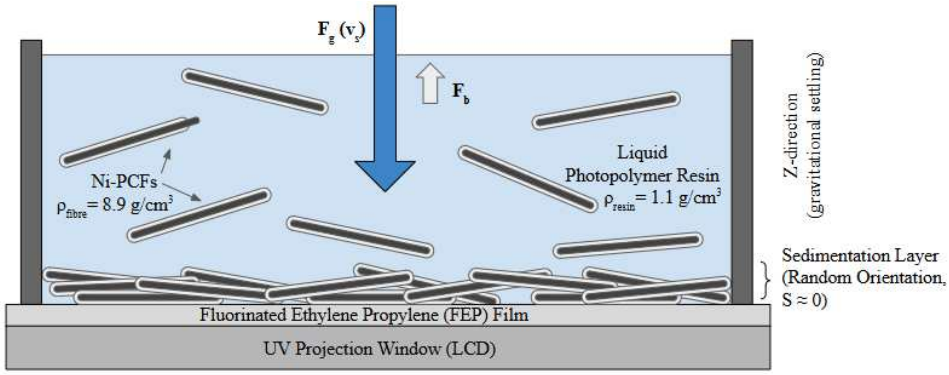


**Fig. 4** Conceptual schematic representation of density-driven particle settling ($v_s$) caused by the large density differential between nickel-coated microfibres ($\rho \approx 8.9$ g/cm$^3$) and the liquid photopolymer resin ($\rho \approx 1.1$ g/cm$^3$).

### 4.3 Failure Mode Analysis ($B < B_{\text{crit}}$)

Experimental processing of Ni-PCFs within the baseline acrylate resin matrix yielded zero macro- or micro-scale directional anisotropy in single-layer samples. Three dominant failure mechanisms account for this operational limit:

- **Field Magnitude Deficit:** Air-core Helmholtz coils constrained by desktop vat photopolymerization spatial envelopes and $I^2R$ thermal dissipation boundaries generate a maximum center flux density of 0.31-0.40 mT. Overcoming dynamic viscous drag in unheated resins ($\eta > 300$ cP) requires magnetic field flux densities exceeding 15-50 mT [9].
- **Particle Agglomeration and Mechanical Interlocking:** Unlike yield-stress composite systems where matrix rheology suppresses clustering prior to field alignment [9], high aspect ratio PCFs form inter-particle mechanical clusters driven by residual van der Waals and magnetic dipole interactions, drastically elevating rotational moment of inertia beyond single-particle kinematic model predictions. Surface functionalization or matrix modification is typically required to suppress these inter-particle attractions during vat photopolymerization [3]. Under applied magnetic fields, magnetic inclusions form vertical chain structures driven by inter-dipolar attraction and magnetic field gradients [5]; however, in low-field setups ($B < B_{\text{crit}}$), these attractive forces exacerbate inter-particle clustering and mechanical interlocking without yielding global fibre orientation.
- **Pre-Cure Gelation Kinetics:** Photopolymer crosslinking and gelation under UV exposure occur faster than the field-driven rotational response time achievable under low-field

conditions ($Mn \gg Mn_{crit}$). Without sufficient field strength or pre-exposure dwell times, rapid resin gelation locks fillers in place before orientation can occur [3].

Macro-scale mechanical and electrical evaluations corroborated the microscopic orientation factor data. Directional surface resistivity measurements taken parallel ($\rho_{\parallel}$) and perpendicular ($\rho_{\perp}$) to the magnetic coil axis yielded equivalent values ($\rho_{\parallel} = 4.2 \times 10^4\ \Omega \cdot \text{cm}$ vs. $\rho_{\perp} = 4.5 \times 10^4\ \Omega \cdot \text{cm}$), confirming an isotropic electrical percolation network. Furthermore, tensile testing of dumbbell specimens printed along both principal coil axes displayed statistically identical elastic moduli ($E_{\parallel} = 1.82 \pm 0.12$ GPa, $E_{\perp} = 1.79 \pm 0.10$ GPa). These bulk isotropic properties conclusively demonstrate that low-field intensities fail to establish functional directional anisotropy in desktop vat photopolymerization setups.

### 4.4 Engineering Design Guidelines for High-Field In-Situ Integration

To overcome the physical, thermal, hydrodynamic, and particulate constraints identified in this framework, future field-assisted vat photopolymerization systems should incorporate the following design paradigms: 1) Replacing air-core Helmholtz geometries with high-permeability C-frame iron cores or optimized Halbach permanent magnet arrays may concentrate flux lines across the active exposure plane to achieve flux densities exceeding 15-50 mT [9]. 2) Unlike thermal post-curing approaches that maintain high ambient viscoelasticity during deposition [10] operating at elevated in-situ thermal windows (40°C-50°C) reduces bulk resin dynamic viscosity ($\eta$) by 50%-70%, significantly decreasing rotational viscous drag ($\tau_{drag}$) without requiring higher electrical current inputs or inducing coil overheating ($I^2R$) [3]. 3) Ultrasonication is a common way to break up agglomerates and promote the dispersion of nanoparticles into a base polymer matrix [11]. Ultrasonic agitation may break up cluster interlocking and therefore reduce effective inter-particle static friction, lowering the rotational energy barrier for field alignment. 4) Addressing rapid gravitational sedimentation by adjusting matrix density or imparting a yield-stress rheology via thixotropic additives like fumed silica or nano-clay platelets [10] or replacing solid nickel shells with lower-density magnetic coatings (such as core-shell magnetite $Fe_3O_4$ nanoparticles) may lower the settling velocity ($v_s$) and maintain uniform fibre suspension during prolonged print cycles. 5) Apply steric surface functionalization (e.g., silane coupling agents) to the PCFs to suppress attractive inter-particle interactions and prevent magnetic agglomeration, ensuring individual fibre kinematics align with single-particle model assumptions [3]. 6) Modifying the print slicing software to introduce a discrete post-dispense, pre-cure dwell stage, where applying the magnetic field during a 3-5 s pause prior to UV LCD exposure allows microfillers to complete rotational orientation before photopolymer gelation kinetics lock the composite matrix [1] [5].

## 5 Conclusion

This technical note detailed the design, hardware integration, and operational physical boundaries of a low-field Helmholtz coil configuration retrofitted to a commercial desktop LCD-VP platform. Although idealized single-particle kinematic models predict sufficient torque for magnetic microfibre orientation, empirical implementation generating 0.31-0.40 mT (24-30 V) achieved negligible directional alignment. In summary, this technical note advances the characterization of

magnetically assisted additive manufacturing by establishing that 1) low-field active magnetic fields generate a statistically verifiable directional bias ($S_{2D} = 0.156 \pm 0.104$) above isotropic controls ($S_{2D} = -0.004 \pm 0.044$), though high spatial variability ($\sigma = 11.16^{\circ} \pm 14.42^{\circ}$) indicates proximity to the lower kinetic threshold for full alignment, and 2) evaluating Gaussian fit accuracy ($R^2 = 0.60 \pm 0.26$) in isolation can be misleading in weak-field regimes; physical anisotropy must be verified using second-order tensor metrics ($S_{2D}$) to accurately gauge microstructural orientation in resin vats.

This rotational limitation is governed by high dynamic viscous drag ($\eta \approx 100\text{-}300$ mPa · s), rapid particle sedimentation (which restricts operation to single layers due to optical opacity), and inter-particle cluster agglomeration occurring well within the photopolymer gelation window. Macro-scale electrical resistivity and tensile testing corroborated these microscopic findings, demonstrating isotropic bulk properties ($S_{2D} \approx 0$). The results conclusively demonstrate that low-field air-core setups are insufficient for in-situ VP operations requiring high directional order. To achieve functional anisotropy in future field-assisted additive manufacturing frameworks, field magnitudes exceeding 15-50 mT, active closed-loop thermal viscosity management, acoustic de-agglomeration, and decoupled pre-exposure dwell routines are strictly required.

## 6 Declarations

**Funding:** The authors declare that no funds, grants, or other support were received during the preparation of this manuscript.

**Conflict of Interest / Competing Interests:** The authors have no relevant financial or non-financial interests to disclose.

**Ethical Approval:** Not applicable.

**Consent to Participate / Publish:** Not applicable.

**Author Contributions:** All authors contributed to the study conception, experimental design, data collection, analysis, and drafting of the manuscript. All authors read and approved the final manuscript.

**Data Availability:** The datasets generated during and/or analyzed during the current study are available from the corresponding author on reasonable request.

## 7 References

**1.** Martin JJ, Fiore BE, Erb RM (2015) Designing bioinspired composite reinforcement architectures via 3D magnetic printing. Nat Commun 6:. https://doi.org/10.1038/ncomms9641

2. Erb RM, Libanori R, Rothfuchs N, Studart AR (2012) Composites Reinforced in Three Dimensions by Using Low Magnetic Fields. Science (1979) 335:199–204. https://doi.org/10.1126/science.1210822

3. Safaee S, Schock M, Joyee EB, et al (2022) Field-assisted additive manufacturing of polymeric composites. Addit Manuf 51:102642. https://doi.org/10.1016/j.addma.2022.102642

4. Bira N, Dhagat P, Davidson JR (2020) A Review of Magnetic Elastomers and Their Role in Soft Robotics. Front Robot AI 7:. https://doi.org/10.3389/frobt.2020.588391

5. Joyee EB, Szmelter A, Eddington D, Pan Y (2020) Magnetic Field-Assisted Stereolithography for Productions of Multimaterial Hierarchical Surface Structures. ACS Appl Mater Interfaces 12:42357–42368. https://doi.org/10.1021/acsami.0c11693

6. Batchelor GK (1970) Slender-body theory for particles of arbitrary cross-section in Stokes flow. J Fluid Mech 44:419–440. https://doi.org/10.1017/S002211207000191X

7. Kubík M, Válek J, Žáček J, et al (2022) Transient response of magnetorheological fluid on rapid change of magnetic field in shear mode. Sci Rep 12:10612. https://doi.org/10.1038/s41598-022-14718-5

8. Hermans JJ, Hermans PH, Vermaas D, Weidinger A (1946) Quantitative evaluation of orientation in cellulose fibres from the X-ray fibre diagram. Recueil des Travaux Chimiques des Pays-Bas 65:427–447. https://doi.org/10.1002/recl.19460650605

9. Kim Y, Yuk H, Zhao R, et al (2018) Printing ferromagnetic domains for untethered fast-transforming soft materials. Nature 558:274–279. https://doi.org/10.1038/s41586-018-0185-0

10. Compton BG, Lewis JA (2014) 3D-printing of lightweight cellular composites. Advanced Materials 26:5930–5935. https://doi.org/10.1002/adma.201401804

11. Shah M, Ullah A, Azher K, et al (2023) The Influence of Nanoparticle Dispersions on Mechanical and Thermal Properties of Polymer Nanocomposites Using SLA 3D Printing. Crystals (Basel) 13:285. https://doi.org/10.3390/cryst13020285